

Dynamics of viscoelastic pipe flow at low Reynolds numbers in the maximum drag reduction limit

By JOSE M. LOPEZ, GEORGE H. CHOUERI,
BJÖRN HOF

Institute of Science and Technology Austria, 3400 Klosterneuburg, Austria

(Printed 11 June 2019)

Polymer additives can substantially reduce the drag of turbulent flows and the upper limit, the so called state of “maximum drag reduction” (MDR), is to a good approximation independent of the type of polymer and solvent used. Until recently, the consensus was that, in this limit, flows are in a marginal state where only a minimal level of turbulence activity persists. Observations in direct numerical simulations at low Reynolds numbers (Re) using minimal sized channels appeared to support this view and reported long “hibernation” periods where turbulence is marginalized. In simulations of pipe flow at Re near transition we find that, indeed, with increasing Weissenberg number (Wi), turbulence expresses long periods of hibernation if the domain size is small. However, with increasing pipe length, the temporal hibernation continuously alters to spatio-temporal intermittency and here the flow consists of turbulent puffs surrounded by laminar flow. Moreover, upon an increase in Wi , the flow fully relaminarises, in agreement with recent experiments. At even larger Wi , a different instability is encountered causing a drag increase towards MDR. Our findings hence link earlier minimal flow unit simulations with recent experiments and confirm that the addition of polymers initially suppresses Newtonian turbulence and leads to a reverse transition. The MDR state on the other hand results at these low Re from a separate instability and the underlying dynamics corresponds to the recently proposed state of elasto-inertial turbulence (EIT).

1. Introduction

The addition of small amounts of polymers to a turbulent flow is known to be one of the most efficient drag reduction technologies. Since its discovery by Toms (1948), it has been extensively used to mitigate friction losses in the pipeline transportation of turbulent fluids. Polymer drag reduction has also become the subject of widespread research aimed at understanding the physics underlying this phenomenon (see e.g. review by White & Mungal 2008). The amount of drag reduction that is achieved increases with increasing polymer concentration, but it eventually saturates at an upper limit known

as the maximum drag reduction (MDR) state. A remarkable feature of this asymptotic limit is that it depends only weakly from the solvent and polymer properties. While first reports on MDR trace back to the seventies (Virk *et al.* 1970), a consensus about the nature of this limit is still lacking. The usual observation of a continuous decrease in the friction factor with increasing polymer concentration and the eventual saturation to MDR has led to the interpretation of MDR as a marginal state of turbulence. However, why turbulence persists and does not fully relaminarise, even though polymers obviously have the tendency to subdue turbulence, has remained an open question.

It has been widely accepted for many years that MDR was a universal state characterized by an empirical logarithmic velocity profile, i.e. the Virk’s ultimate profile (Virk *et al.* 1970). This motivated various theoretical efforts to derive the supposedly universal profile (see e.g. L’vov *et al.* 2004; Benzi *et al.* 2006). However, there is growing evidence that the mean velocity profile at MDR is neither logarithmic nor universal (White *et al.* 2012; Elbing *et al.* 2013; White *et al.* 2018). A number of phenomenological theories based on either the viscous or elastic behaviour of the polymers have also been postulated to explain the MDR phenomenon. It has been for example speculated that MDR might occur when the elastic energy stored in the polymers becomes comparable to the flow kinetic energy and polymers affect all flows scales (Sreenivasan & White 2000). Another relevant theory was introduced by Warholic *et al.* (1999), who proposed that MDR takes place when the Reynolds shear stresses vanish, i.e. the self-sustaining mechanism of Newtonian turbulence is fully suppressed, and the flow is fully dominated by polymer stresses. Nevertheless, none of these phenomenological theories has so far been entirely supported. More recent theories are based, to a large extent, on direct numerical simulations using the FENE-P (finitely extensible nonlinear elastic-Peterlin) model to describe the polymers dynamics. While the high computational cost of viscoelastic simulations has limited numerical studies to low-to-moderate Reynolds numbers, MDR occurs even at Reynolds numbers just past transition, and so these studies offer valuable insights into the nature of this phenomenon.

The interpretation of MDR as a marginal turbulent state has recently found support in simulations performed by Xi & Graham (2010*a,b*, 2012*a,b*), henceforth referred to as X&G, using minimal channels and a low Reynolds number ($Re = 3600$). These authors observed that viscoelastic turbulence is characterized by the alternation between intervals of high and low friction. The latter intervals, which they called hibernating turbulence, were found to share several structural and statistical features with MDR. Since the frequency and duration of these intervals increased gradually with increasing polymer elasticity, they proposed that MDR might be a marginal state of hibernating turbulence whose energy cannot be further reduced by polymer activity. An alternative explanation to the MDR phenomenon was given by Samanta *et al.* (2013). By combining experiments in pipe flow and simulations in channel flow, they reported the existence of a secondary instability driven by the interplay between elasticity and inertia at high polymer concentration. Such instability, which was called elasto-inertial instability (EII),

sets in at Reynolds numbers below those at which the transition to turbulence occurs in Newtonian flows, providing an explanation to the early turbulence phenomenon often observed in experiments (Ram & Tamir 1964; Little & Wiegard 1970). In addition, the experiments showed that the friction factor associated with the state resulting from the EII, named elasto-inertial turbulence (EIT), agrees well with that of MDR. On this basis, the authors suggested that turbulent drag reduction is eventually limited by the EII, which prevents flows from relaminarising, and that the observed MDR friction factor values are simply the natural drag levels of EIT.

To test these theories, Choueiri *et al.* (2018), hereafter C,L&H, investigated the effect of increasing the polymer concentration on turbulent pipe flow in experiments at constant Reynolds numbers. Surprisingly, for not too large Reynolds numbers ($Re < 4000$), the addition of polymers resulted in full relaminarisation. Here, shear rates and concentrations were moderate, so that the EII had not occurred yet while Newtonian turbulence was fully suppressed. Further addition of polymers, however, destabilised the laminar flow and triggered the EII. Subsequently, the drag increased and MDR was approached from the laminar limit. This scenario strongly suggests that MDR is a state disconnected from Newtonian turbulence, thereby supporting the theory that MDR is caused by the EII. On the other hand, the authors observed that prior to relaminarisation the flow becomes spatio temporally intermittent and consists of slugs and puffs. This is in principle in line with the temporal intermittency observed by X&G. The main difference is that they proposed that the low drag (or hibernating) phases correspond to the eventual MDR state, whereas the intermittency in time and space observed by C,L&H is part of a reverse transition and not the asymptotic state. To clarify this point, we carry out direct numerical simulations of viscoelastic pipe flow at a similar Reynolds number ($Re = 3500$), using short streamwise domain length (twice as long as in X&G), and following a path in parameter space comparable to that of C,L&H. As will be shown below, the dynamical scenario is in good agreement with that of X&G in that low drag periods become longer and longer and appear to approach some asymptotic level as the Weissenberg number (Wi) increases. However, for even larger Wi , the flow abruptly relaminarises.

Moreover, when the small computational domain is increased to more realistic sizes, i.e. pipe lengths sufficiently large to contain a puff, the temporal intermittency changes to spatio-temporal intermittency, revealing that, as reported in the experiments by C,L&H, indeed, a reverse transition occurs with increasing Wi . At the same time, the approach towards an almost constant drag level reported by X&G, and also found in the small domains in the present study, does not persist in the large domains. Instead, the flow returns to intermittent puffs and subsequently fully relaminarises. For even larger Wi , an instability occurs that, like in the experiments, leads to a separate fluctuating dynamical state. Our computations hence qualitatively agree with the experiments of C,L&H. While the dominant flow structures reported in experiments of EIT are large scale streamwise streaks (Choueiri *et al.* 2018), in simulations of EIT (Samanta *et al.* 2013; Dubief *et al.* 2013) only small near wall spanwise oriented vortical structures were found. In the present

case we find the same near wall spanwise vortical structures. These structures are found to be localised and they give rise to large scale streamwise streaks, similar to those observed in experiments.

2. Problem formulation and numerical methods

We investigate numerically the dynamics of a dilute polymer solution flowing through a straight circular pipe at a constant flow rate. Polymer dynamics is modeled using the FENE-P model (Bird *et al.* 1980). Individual polymer molecules are represented in this model as two inertialess spherical beads connected by a straight non-linear spring. The orientation and elongation of each polymer molecule is determined by the end-to-end vector \mathbf{q} connecting the two beads. The ensemble average of the tensor product of all end-to-end vectors defines a positive-definite symmetric polymer conformation tensor, $\mathbf{C} = \langle \mathbf{q} \otimes \mathbf{q} \rangle$, which allows the problem to be formulated from a continuum medium approach.

2.1. Governing equations and dimensionless parameters

The governing equations are presented directly in dimensionless form. The pipe radius R , the laminar centreline velocity u_{lc} and the dynamic pressure ρu_{lc}^2 were chosen as characteristic scales for length, velocity and pressure respectively. \mathbf{q} was normalized with $\sqrt{kT_e/H}$, where k denotes the Boltzmann constant, T_e is the absolute temperature and H is the spring constant. The maximum polymer extension is indicated by the dimensionless parameter $L = q_0/\sqrt{kT_e/H}$, where q_0 is the maximum separation between beads allowed by the spring. Cylindrical coordinates (z, θ, r) are used.

The temporal evolution of \mathbf{C} is obtained by solving the following constitutive equation

$$\partial_t \mathbf{C} + \mathbf{v} \cdot \nabla \mathbf{C} = \mathbf{C} \cdot \nabla \mathbf{v} + (\nabla \mathbf{v})^T \cdot \mathbf{C} - \boldsymbol{\tau}, \quad (2.1)$$

where $\mathbf{v} = (u, v, w)$ is the velocity vector field and $\boldsymbol{\tau}$ is the polymer stress tensor. The first two terms on the right hand side of equation (2.1) model polymer stretching due to hydrodynamic forces, whereas $\boldsymbol{\tau}$ represents the relaxation forces bringing the polymers back to its equilibrium configuration. $\boldsymbol{\tau}$ is computed using the Peterlin closure

$$\boldsymbol{\tau} = \frac{1}{Wi} \left(\frac{\mathbf{C}}{1 - \frac{tr(\mathbf{C})}{L^2}} - \mathbf{I} \right), \quad (2.2)$$

where $tr(\mathbf{C})$ denotes the trace of the polymer conformation tensor, \mathbf{I} is the unit tensor and Wi is the Weissenberg number; a dimensionless number quantifying the ratio of the polymer relaxation time λ to the characteristic flow time scale R/u_{lc} .

The fluid motion is governed by the continuity and Navier-Stokes equations

$$\nabla \cdot \mathbf{v} = 0, \quad (2.3)$$

$$\partial_t \mathbf{v} + \mathbf{v} \cdot \nabla \mathbf{v} = -\nabla P + \frac{\beta}{Re} \nabla^2 \mathbf{v} + \frac{(1-\beta)}{Re} \nabla \cdot \boldsymbol{\tau} + \frac{4(1+\alpha)}{Re} \hat{e}_z, \quad (2.4)$$

where P is the pressure, $\beta = \nu_s/\nu$ measures the relative importance between the sol-

vent viscosity ν_s and the viscosity of the solution at zero shear rate ν , $Re = u_{ic}R/\nu$ is the Reynolds number and α is the fluctuating pressure gradient required to keep a constant mass flux. Polymers modify the dynamics of Newtonian flows through polymer stresses. These are incorporated into the conventional Navier-Stokes equation through the divergence of the polymer stress tensor. The $(1 - \beta)$ prefactor multiplying this term indicates the contribution of the polymers to the total viscosity and must be small for a dilute polymer solution. Periodic boundary conditions are used in the streamwise z and azimuthal θ directions, whereas the no-slip condition is imposed at the pipe wall $r = R$.

In all simulations presented in this paper the Reynolds number was fixed to $Re = 3500$, for which the flow is turbulent in the Newtonian case, and Wi was used as control parameter. We also fixed β to 0.9 which is the value corresponding to the experiments of C,L&H at a concentration of 90 ppm. Given the values of β and L , polymers can be characterized by their extensibility number $E_x = 2L^2(1 - \beta)/3\beta$ (Xi & Graham 2010b). For our simulations we have considered two different polymers with very different extensibilities. The maximum extension of the first polymer type, $L = 30$, was chosen so that its extensibility number, $E_x = 66.6$, coincides with one of the cases presented in Xi & Graham (2010b). The second polymer type has a very high extensibility, $E_x = 2962.96$ for $L = 200$, and it corresponds to the parameters used in simulations of elasto-inertial turbulence by Dubief *et al.* (2013). These two cases will be henceforth referred to as moderate extensibility ME and large extensibility LE cases respectively.

2.2. Numerical methods

The governing equations are solved in primitive variables using a highly scalable pseudo-spectral solver recently developed in-house. The code is parallelized using a combination of the MPI and OpenMP programming models (see Shi *et al.* 2015, for further details). Spatial discretization in the two periodic directions, z and θ , is accomplished via Fourier-Galerkin expansions, whereas central finite differences on a Gauss-Lobatto-Chebyshev grid are used in r . Pressure and velocity in equation (2.4) are decoupled through a Pressure Poisson Equation (PPE) formulation. An influence matrix is used to impose the free divergence boundary condition directly on velocity, thereby avoiding the use of artificial pressure boundary conditions. The equations for the azimuthal and radial velocity components v and w are decoupled using the change of variables, $u_+ = w + iv$ and $u_- = w - iv$ (Orszag & Patera 1983).

The time integration was carried out using a second order accurate predictor-corrector scheme based on the Crank-Nicolson method (Willis 2017). For a generic variable \mathbf{X} at a time n the predictor equation reads

$$\left(\frac{1}{\delta t} - ic\nabla^2\right)\mathbf{X}_1^{n+1} = \left(\frac{1}{\delta t} + (1 - ic)\nabla^2\right)\mathbf{X}^n + \mathbf{N}^n, \quad (2.5)$$

where \mathbf{N} denotes the non-linear terms, δt is the time step size and the constant ic defines the implicitness of the method ($ic = 0.5$ in our simulations). The initial estimate \mathbf{X}_1^{n+1} is then refined following an iterative correction procedure. At each corrector iteration the

Section	pipe length (R)	m_r	m_θ	m_z
§3 ($S_c = 0.5$)	10	64	64	128
§3 ($S_c = 2$)	10	128	128	256
§4	20	64	64	256
§4	40	64	64	512
§4	100	64	64	1280
§5 (EIT)	10	64	100	256
§5 (EIT)	40	64	100	1280

TABLE 1. Number of radial nodes, m_r , and Fourier modes, m_θ and m_z , used in the simulations.

non-linear terms are re-evaluated and \mathbf{X}_j^{n+1} is obtained solving the following equation

$$\left(\frac{1}{\delta t} - ic\nabla^2\right)\mathbf{X}_{k+1}^{n+1} = \left(\frac{1}{\delta t} + (1 - ic)\nabla^2\right)\mathbf{X}^n + ic\mathbf{N}_k^{n+1} + (1 - ic)\mathbf{N}^n, \quad (2.6)$$

where $k = 1, 2, \dots$. The iteration loop stops when $\|\mathbf{X}_{k+1}^{n+1} - \mathbf{X}_k^{n+1}\| \leq 10^{-6}$. Convergence usually occurs after one iteration of the corrector step. The additional computational cost of computing the advective terms twice at each time step is compensated by the larger δt allowed by this temporal scheme in comparison with other conventional methods. The source terms in equation (2.1) and the term containing the divergence of the polymer stress tensor in equation (2.4) are treated as non-linear terms. Note that equation (2.1) is hyperbolic and does not have any diffusive term ($\nabla^2\mathbf{X}$). This lack of dissipation leads to numerical error accumulation which often causes spurious instabilities and numerical breakdown. To avoid these problems we incorporate a small amount of artificial diffusion to our simulations which enhances numerical stability. This is accomplished by adding a laplacian term $\frac{1}{ReS_c}\nabla^2\mathbf{C}$ to the right hand side of equation (2.1), where $S_c = \nu/\kappa$ is the Schmidt number quantifying the ratio between the viscous and artificial diffusivities. Unless otherwise specified, the simulations presented in this paper were performed using $S_c = 0.5$. This yields an artificial diffusion coefficient $\frac{1}{ReS_c} \sim O(10^{-4})$ which is of same order of magnitude as in Xi & Graham (2010b), and quite below those of early works, e.g. Ptasinsky *et al.* (2003); Sureshkumar *et al.* (1997), where $\frac{1}{ReS_c} \sim O(10^{-2})$. With the inclusion of this laplacian term two boundary conditions are needed: as suggested in Beris & Dimitropoulos (1999) we impose that \mathbf{C} at $r = R$ must be the same as without artificial diffusion, whereas symmetry boundary conditions are used at $r = 0$.

The numerical resolution of the simulations presented in this paper is shown in table 1. δt is dynamically adjusted to ensure that the Courant-Friedrichs-Lewy (CFL) condition always remains below 0.25.

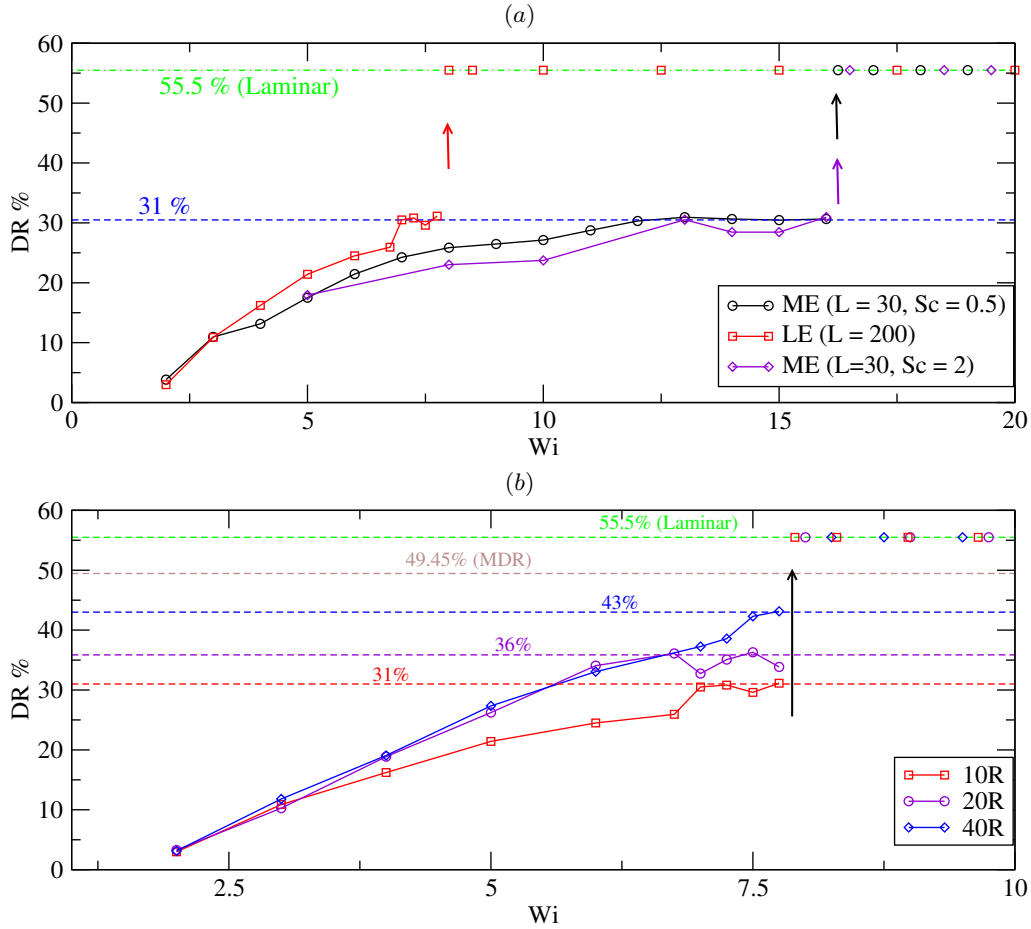


FIGURE 1. (Color online) Evolution of the drag reduction percentage $DR\%$ with increasing Wi up to relaminarisation occurs in pipe flow simulations performed at $Re = 3500$. (a) Simulations carried out in a $10R$ long pipe using two polymers with different extensibilities: LE (large extensibility, $L = 200$) and ME (moderate extensibility, $L = 30$). Diamonds (purple line) illustrate the effect of reducing the global artificial diffusion. (b) Variation of $DR\%$ as the pipe length is varied for the LE case. The green and brown dashed lines show the drag reduction level of the laminar and MDR states, respectively, whereas the remaining dashed lines indicate the maximum drag reduction achieved in each case. Arrows indicate the Wi at which flow relaminarisation occurs.

3. Dynamics of viscoelastic pipe flow turbulence in short computational domains

Because of the additional equations for C and τ , viscoelastic turbulence simulations are in computational terms far more demanding than Newtonian simulations. A common approach to minimise the computational cost is to choose the smallest domain size that computes reasonably accurate dynamics. On that basis, we have set the pipe length to $L_z = 10R$, which is nearly the minimum size needed in Newtonian pipe flow simulations to ensure that these are unaffected by streamwise periodicity. The simulations were performed according to the following procedure. Starting from a fully turbulent

Newtonian solution, we increased Wi progressively by one unit, with the exception of the range $6 \leq Wi \leq 8$ in the LE case, where Wi was varied in intervals of 0.25. The simulations were run over $2000R/u_{lc}$ time units and as initial condition we used a previously computed solution with Wi close to that being computed. The averaged drag reduction percentage was calculated as $DR\% = \frac{f_N - f}{f_N}$, where f_N and f are the average friction factors for the Newtonian and viscoelastic cases respectively. The former is given by the Blasius friction law, $f_N = 0.079Re^{-0.25}$, whereas the latter is calculated from the Fanning friction formula, $f = \frac{\tau_w}{2\rho U_b^2}$, where U_b , τ_w and ρ are the bulk velocity, average wall shear stress and fluid density respectively. For each Wi , a set of 10 simulations was performed and the drag reduction level was computed by averaging over the ensemble of the simulations.

As shown in figure 1 (a), even for two simulations mimicking different polymers, the same qualitative scenario in terms of drag reduction is obtained. The amount of drag reduction increases continuously with increasing Wi up to a critical threshold after which the flow relaminarises. A clear effect of increasing the maximum polymer extension L is that the dynamics are accelerated: the polymer with higher extensibility LE produces for the same Wi significantly larger drag reduction than the ME polymer, and it eventually causes relaminarisation at a much lower value of Wi , $Wi_{lam} = 7.75$, than in the ME case, $Wi_{lam} = 16$. We note here that, as Wi_{lam} is approached, the simulations become sensitive to the initial condition and turbulence does not always survive over the time threshold chosen. The critical values for relaminarisation Wi_{lam} given above correspond to the highest values of Wi for which turbulence survives in more than 50% of the simulations performed. There are also certain ranges of Wi at which polymer extensibility does not appear to play any role. For example, at very low Wi ($W \leq 3$), the degree of polymer stretching is low and both polymers, despite having very different extensibility, produce nearly the same drag reduction. A much more surprising effect occurs at larger Wi prior to relaminarisation. Here, the drag reduction approaches an almost constant level, 31%, regardless of the polymer extensibility. This levelling off was observed in the earlier study of Xi & Graham (2010b) and suggested as an asymptotic regime (AR). In the present study, the AR occurs over a narrow range of Wi , and since dynamical changes take place faster for higher extensibility, it is much more evident in the ME case, $12 \leq Wi \leq 16$, than in the LE case, $6.75 \leq Wi \leq 7.75$.

A key feature of the dynamics in these simulations is the presence of temporal intermittency, with periods of low friction which are interspersed with other periods of higher friction, as shown in figure 2. These intermittent dynamics are also in agreement with the simulations of Xi & Graham (2010b, 2012b), who dubbed the low and high friction intervals as hibernating and active turbulence, respectively. The frequency and duration of hibernating events increases progressively with increasing Wi , and the friction associated with active turbulent events decreases as Wi increases, leading to the gradual growth in average drag reduction shown in the figure 1 (a). To further illustrate the distinction between hibernating and active turbulence, the bottom panel in figure 2 shows

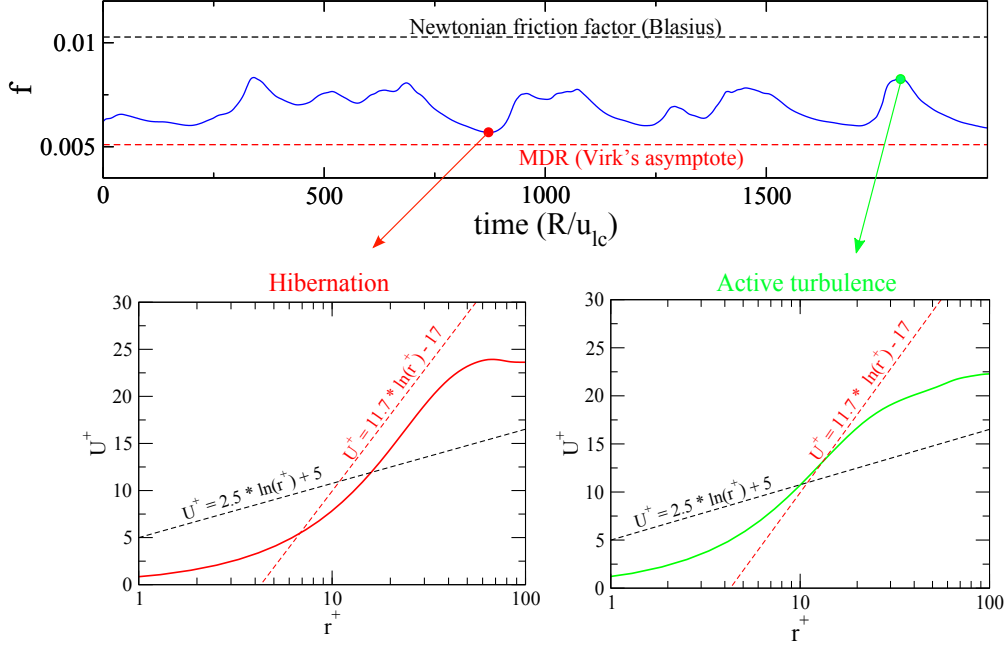


FIGURE 2. (Color online) Temporal intermittency. The top panel shows the temporal evolution of the friction factor f for the ME case and $Wi = 13$, whereas the bottom panels illustrate instantaneous mean velocity profiles at low and high friction events. Note that here velocity (U^+) and radius (r^+) are expressed in inner units, i.e. normalized with the friction velocity ($u_\tau = \sqrt{\tau_w/\rho}$) and the viscous length ($\delta_\nu = \nu/u_\tau$) respectively.

instantaneous velocity profiles in inner units corresponding to each state. The black and red dashed lines in these figures show the logarithmic laws that have been traditionally used to describe the mean velocity profile in the logarithmic layer ($30 \lesssim r^+ \lesssim 60$, for $Re = 3500$) for wall bounded Newtonian turbulence (Prandtl-Kármán law) and viscoelastic turbulence at MDR (Virk's asymptote), respectively. It should be noted that the functional form of the mean velocity profile at MDR is not truly logarithmic (White *et al.* 2012; Elbing *et al.* 2013) and so the Virk's asymptote should be understood as an idealization of velocity profiles in this limit. Hibernating events are characterized by velocity profiles that notably deviate from the Prandtl-Kármán law and become nearly parallel to the Virk's asymptote profile throughout the logarithmic layer. By contrast, in active turbulence events, although friction may be substantially lower than that for pure Newtonian turbulence, the profile in the log layer has a comparable slope to the Prandtl-Kármán law. On the basis of similar observations, it has been argued that states of active turbulence have similar properties to Newtonian turbulence, whereas hibernating events could be directly connected to MDR. More specifically, it was suggested that MDR might be a state fully dominated by hibernation, which is achieved asymptotically as Wi is increased (Xi & Graham 2010*a*). However, in our simulations, as well as in previous simulations reporting this intermittent scenario, the flow eventually relaminarises

with increasing Wi and an asymptotic state (the AR) is reached only over a narrow range of Wi prior to relaminarisation. Since the AR exhibits some features of MDR: saturation of the drag reduction level with increasing Wi and comparable results are obtained for different polymer properties, it has been interpreted as the first numerical evidence of MDR. However, there is also evidence which appears to indicate that the AR does not correspond to MDR. Firstly, while hibernation is prominent in this regime, active turbulence events also occur frequently, and so the average drag reduction level at AR (31%) is considerably less than that of MDR at $Re = 3500$ (49.5%). Another distinctive feature is that in the AR the saturation of drag reduction occurs over a finite range of Wi and upon further increase in Wi the flow relaminarises. In contrast, MDR is a persistent state and the drag reduction level remains nearly unchanged as Wi increases. Finally, it should also be noted that temporal intermittent dynamics such as those previously described have not been reported in experiments at MDR. It is therefore unclear whether the dynamics of the AR may be related to MDR.

Before proceeding further, we want to briefly discuss the impact that the artificial diffusion added to equation 2.1 has on the reported scenario. Sid *et al.* (2018) recently showed that adding polymer diffusion substantially weakens the elastic scales at large Wi . They found that this effect is particularly relevant in the elasto-inertial turbulent regime, where elastic scales play a crucial role in feeding turbulence and thus an excessive polymer diffusion leads to flow relaminarisation. As will be shown later, the simulations described in this section do not correspond to the elasto-inertial regime. However, it is important to clarify whether the relaminarisation observed might also be an artifact of the artificial polymer diffusion. If the relaminarisation were caused by the diffusive term, one would expect that as S_c is increased, i.e. as the amount of diffusion is reduced, the relaminarisation threshold would progressively shift towards larger values of Wi , until eventually, at a sufficiently large S_c , the relaminarisation does not take place any more. To examine how the polymer diffusion affects the relaminarisation threshold, simulations for the case of moderate extensibility, decreasing the amount of diffusion by a factor of 4 ($S_c = 2$), were performed following the same procedure described above. As seen in figure 1 (a) (diamonds), the flow relaminarisation in these simulations was found to occur at the same value of Wi ($Wi_{lam} = 16$) as in the simulations using $S_c = 0.5$. This insensitivity of the relaminarisation threshold to changes in S_c suggests that the relaminarisation phenomenon is not driven by polymer diffusion but rather a robust feature of these simulations. We also note that, while quantitative differences exist between simulations with $S_c = 0.5$ and $S_c = 2$, i.e. less polymer diffusion produce less drag reduction, the same qualitative scenario is observed in both cases: the amount of drag reduction increases with increasing Wi up to a regime is reached (the AR) where it remains nearly constant. Based on these observations, we argue that polymer diffusion only has a moderate influence at these Wi and does not affect significantly the results discussed in this paper.

4. Simulations in larger computational domains: reverse transition

To assess the influence of the pipe length in the results of § 3, the same computational procedure was repeated using larger pipes ($20R$ and $40R$). A comparison of the drag reduction scenario obtained for the LE polymer when the pipe length was varied is shown in figure 1 (*b*). A first interesting observation is that, consistent with other works on viscoelastic turbulence (Li *et al.* 2006; Wang *et al.* 2017), viscoelasticity increases the streamwise correlation length with respect to Newtonian simulations. Hence, while at these low Re a streamwise length of $10R$ is enough to obtain realistic statistics in Newtonian pipe flow, viscoelastic simulations are still affected by streamwise periodicity and result in lower drag reduction than those obtained when larger pipes are used. Simulations performed in $20R$ and $40R$ long pipes produce nearly the same drag reduction up to $Wi \sim 6.75$, but differ both quantitatively and qualitatively when relaminarisation is approached. For simulations using a $20R$ long pipe, the same qualitative scenario as in the $10R$ long pipe simulations is found: the drag reduction remains nearly constant over a finite range of Wi , $6 \leq Wi \leq 8$, before relaminarisation takes place. However, when a pipe of $40R$ is used, this AR disappears and the drag reduction increases monotonically with increasing Wi until the flow relaminarises. This observation suggests that rather than being a manifestation of MDR, the AR might be a consequence of the streamwise periodicity imposed in the simulations and thus it might lack practical significance.

An additional test to confirm that the dynamics at the AR is different from that at MDR is to compare the flow structures in our simulations with recent experimental visualizations of MDR structures in pipe flow at low Reynolds numbers (Choueiri *et al.* 2018). These experiments showed that turbulence at MDR substantially differs from Newtonian type turbulence and it is characterized by very elongated streaks which are slightly inclined away from the wall (see figure 3 in Choueiri *et al.* (2018)). If the dynamics at the AR corresponded to MDR, similar flow structures should be observed in our simulations, provided that the computational domain is long enough to accommodate them. To examine this possibility, we have performed a new set of simulations using a pipe of $100R$ in axial direction, which is approximately twice the size of the shortest structures observed by Choueiri *et al.* (2018). Figure 3 illustrates the dynamical evolution of the turbulence structures as Wi was increased in these simulations. It shows, at a certain time instant, the variation of the centreline velocity u_c along the pipe (top panel) and isocontours of the radial velocity w (bottom panel) for several Wi representative of different dynamical regimes in the ME case. Note that a Newtonian case (fig. 3 (*a*)) has also been included for comparison. At low drag reduction ($Wi < 6$), the dynamics is very similar to that of the Newtonian case (see panels (*a*) and (*b*) in the figure). Turbulence always fills the pipe entirely and the centreline velocity exhibits comparable fluctuation levels in both cases. Nevertheless, the flow structures in the viscoelastic case are broader and slightly more elongated in the axial direction than those in pure Newtonian turbulence, reflecting the drag reduced nature of the flow in viscoelastic simulations. Another clear distinction is that, while turbulence extends across the entire pipe diameter in the

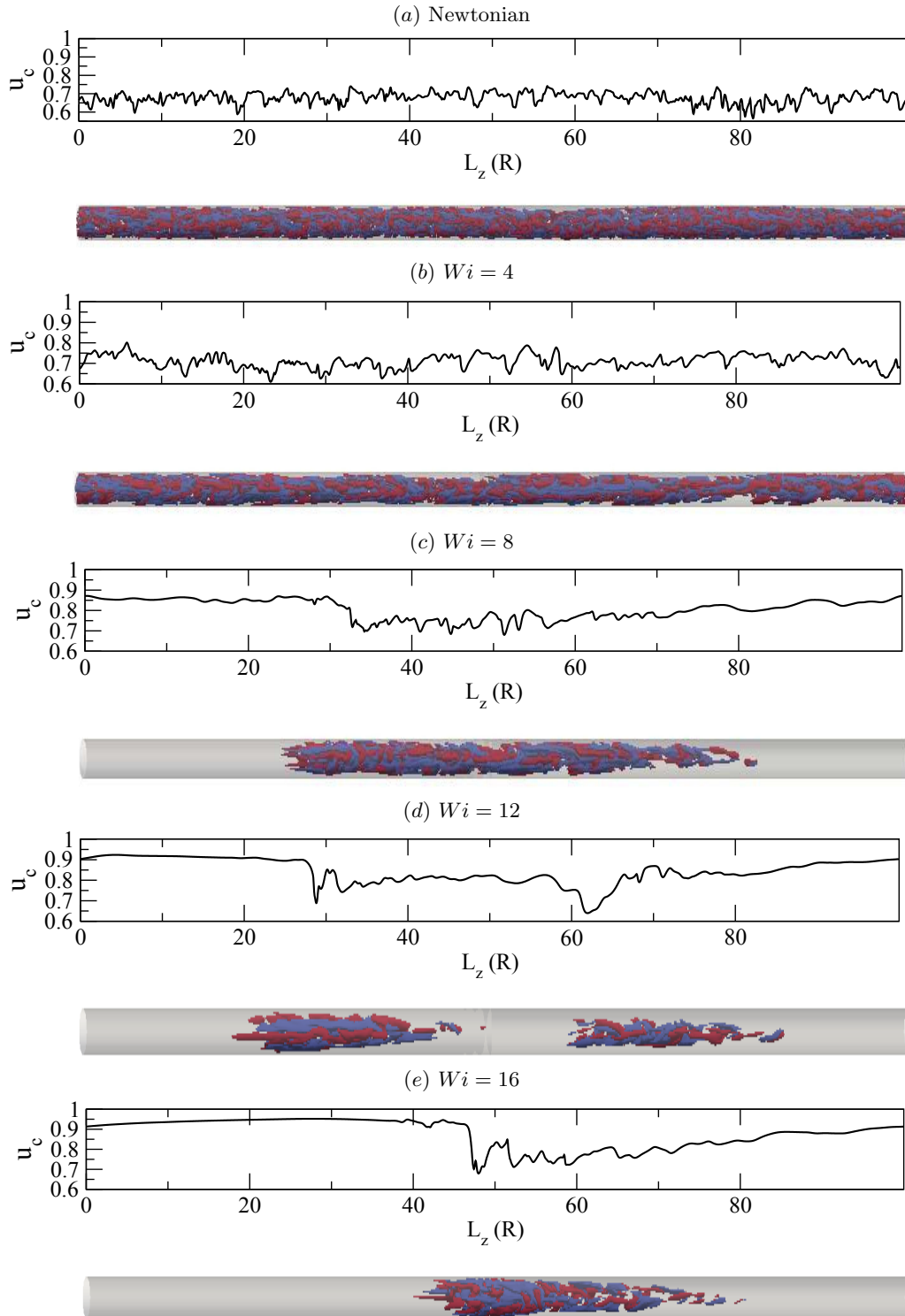


FIGURE 3. (Color online) Evolution of the spatio-temporal dynamics and turbulence structures as Wi increases when the simulations are carried out in a long pipe of $100R$ in the streamwise direction. The upper panel shows the streamwise variation of the centreline velocity, u_c , whereas the lower panel illustrates isosurfaces of the radial velocity. The flow direction is from left to right. Note that the aspect ratio of the pipe has been increased to facilitate visualisation of the structures.

Newtonian case, there are several areas in the drag reduced flow where the near wall turbulence has been suppressed by polymer activity. As Wi increases (between $Wi = 7$ and 11), the dynamics exhibit a complex spatio temporal behaviour. As shown in fig. 3 (c) for $Wi = 8$, turbulence is confined to streamwise localised patches known in the Newtonian pipe flow literature as *slugs*. The distance between the turbulent fronts, i.e. the interfaces separating laminar from turbulent flow, increases progressively with time until the turbulence eventually fills the entire pipe. This space-filling turbulent state does not persist long and turbulence takes back the form of *slugs*, thereby restarting the cycle again. With further increase in Wi , coinciding with those Wi at which the AR occurs in shorter pipes, $12 \leq Wi \leq 16$, turbulence becomes permanently localised in the streamwise direction taking the form of turbulent *puffs*. As seen in fig. 3 (e), these viscoelastic *puffs* are very similar to Newtonian *puffs*: arrow-headed structures where turbulence is mainly concentrated in the sharp upstream edge and progressively diffuses away as the puff is followed downstream. Unlike *slugs*, *puffs* keep their size constant and travel downstream at a nearly constant speed. We also found that these *puffs* sporadically split into two smaller *puff*-like structures (see fig. 3 (d)). However, since the domain is not large enough to contain two full-size *puffs*, there is a strong interaction between them which causes the downstream *puff* to quickly relaminarise (Hof *et al.* 2010). We note here that, although the pipe length in these simulations is enough to identify spatially localized structures, these are still affected by the finite size of the computational domain. As a result, laminar flow is not fully recover, i.e. the centreline velocity does not recover its laminar value $u_c = 1$, and the length of the simulated puffs is slightly shorter than that in laboratory experiments. Finally, when Wi is increased above 16 the flow fully relaminarises, showing that this is a robust feature of these simulations which occurs at the same Wi regardless of the pipe length considered.

The dynamical scenario described above raises two important points. Firstly, increasing Wi in these simulations leads to a relaminarisation scenario which follows the same sequence of states as the transition to turbulence in the Newtonian case but in reverse direction, i.e. turbulence, slugs, puff splitting, puffs and laminar flow. We will henceforth refer to the dynamics of this relaminarisation scenario as reverse transitional dynamics. Secondly, the dynamics at the Wi corresponding to the AR, $12 \leq Wi \leq 16$, is characterized by *puffs* and this is qualitatively very different from the structures observed at MDR in experiments. It should, however, be noted that the reported scenario only occurs at Re near the turbulence transition and so the conclusions reached from these results strictly apply only in this regime.

Finally, we note that a comparison between temporal dynamics in small (minimal) domains and spatio-temporal dynamics in larger domains at similar Reynolds numbers was also presented in Wang *et al.* (2017). This study established the similarity between statistics obtained from time series analysis in minimal domains and those obtained by thresholding and conditional average in larger domains. Nevertheless, the axial length for the large domain simulations in this study was fixed to $L_z \sim 40h$ (h is the channel half-

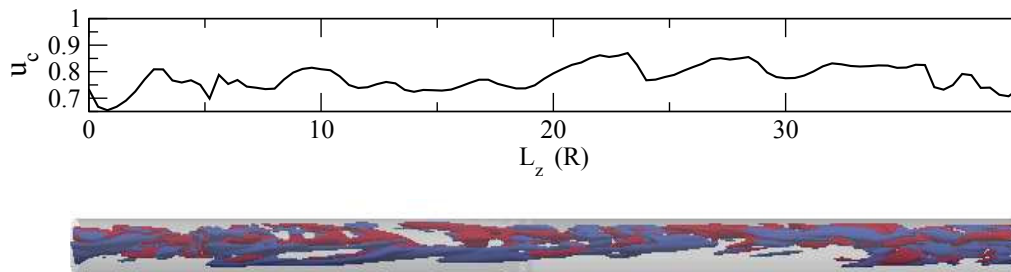


FIGURE 4. (Color online) Same as in figure 3 (e) when a pipe of $40R$ in the streamwise direction is used.

width, equivalent to R in our simulations) and thus the effect of further increasing L_z was not assessed. When using similar computational domains ($L_z = 40R$), our simulations reveal that the flow is significantly affected by finite-size effects. The pipe length here is smaller than the axial extent of the turbulent patches shown in figure 3. Hence, using periodic boundary conditions create artificial interactions between the upstream and downstream edges of these turbulent structures. This results in flow states characterized by space-filling turbulence whose intensity varies in space and time, which are similar to those analysed in Wang *et al.* (2017). An example of these states is shown in figure 4, corresponding to a simulation for $Wi = 16$ using a $40R$ long pipe. In contrast to the simulation in a $100R$ long pipe (figure 3 (e)), where a clear puff is observed, here the flow does not exhibit laminar regions and significant velocity fluctuations coexist with regions of weaker fluctuations along the entire pipe. We argue that, as occur in our simulations, if the simulations presented in Wang *et al.* (2017) were extended to larger axial domains, the spatio-temporal alternation between hibernating and active turbulent regions described in this paper might turn into the coexistence of fully laminar and turbulent flow regions.

5. Comparison with experimental results

The question now is whether the reverse transitional dynamics captured by our simulations provides a meaningful description of viscoelastic pipe flow dynamics, i.e. whether or not these simulations reproduce experimental observations. To answer this question we provide in this section a detailed description of the dynamical scenario found by Choueiri *et al.* (2018) in pipe flow laboratory experiments at a similar Reynolds number, $Re = 3150$, when the polymer concentration c is increased progressively from Newtonian turbulence to MDR (for details about the experimental setup, see supplementary material in Choueiri *et al.* (2018)). Note that the control parameter in these experiments is polymer concentration, whereas in simulations it is the polymer relaxation time λ , i.e. Wi , that varies. These two magnitudes are however directly correlated. It has been shown that even in dilute polymer solutions the relaxation time grows with increasing polymer concentration (Giudice *et al.* 2017). Hence, increasing Wi in our simulations is related to increasing polymer concentration in experiments. Figure 5 (a) shows the

variation of the drag reduction percentage as polymer concentration was varied in the experiments. Similarly to what occurs in the simulations, the amount of drag reduction $DR\%$ increases initially with increasing polymer concentration until a threshold value is reached, $c \sim 23$ ppm (parts per million by weight), at which the flow fully relaminarises. The flow remains laminar regardless of the imposed perturbations over a significant range of polymer concentration ($c \sim 23 - 43$ ppm). However, for $c > 43$ ppm, the flow becomes chaotic again and the drag reduction level approaches progressively that of the Virk's asymptote.

Panels (b) to (f) in figure 5 illustrate how the dynamics change as the polymer concentration increases. More specifically, these figures show the temporal variation of the centreline velocity u_c obtained from LDV measurements at a central streamwise location. The x-axis has been inverted to facilitate comparison with the instantaneous streamwise distribution of u_c shown in figure 3. Note that, as in the simulations, u_c is normalized with the centreline velocity of the laminar state. In the absence of polymers (see figure 5 (b)) the flow is fully turbulent and u_c exhibits persistent random amplitude fluctuations. As the polymer concentration is increased ($c \geq 13$ ppm), time intervals where u_c strongly fluctuates alternate with others at which it nearly recovers its laminar value (see figure 5 (c) and compare to the analogous case in the simulations, figure 3 (c)). This temporal intermittency between turbulent and laminar states indicates that the dynamics at this regime is characterized by spatially localized structures. Furthermore, since the duration of these turbulent and laminar intervals is highly variable, and both trailing and leading edge interfaces show a sharp adjustment of the centreline velocity, it is evident that these localised structures correspond to *slugs* (Wynanski & Champagne 1973). With further increase in concentration ($c \geq 18$ ppm), *slugs* are replaced by *puffs* (see figure 5 (d) and analogous case in the simulations, figure 3 (e)). These structures are clearly distinguishable because of their long diffusive tail and sharp velocity variation associated with the upstream edge. As occurs in the simulations (figure 3 (d)), splitting events are also frequently encountered in the experiments (see figure 5 (e)), leading either to the emergence of *slugs* or trains of *puffs* depending on the polymer concentration. When $23 \text{ ppm} < c < 43 \text{ ppm}$, turbulence is fully suppressed by the polymers and u_c remains constant and equal to the laminar value. It should be emphasized at this point that the dynamics taking place in the experiments is in excellent qualitative agreement with the reverse transition found in the simulations. Ultimately, for $c \geq 43$ ppm (see fig. 5 (f)), the flow reaches MDR and u_c exhibits again persistent oscillations. The frequency and amplitude of these oscillations are however much lower than those for a fully turbulent Newtonian flow, and the deviation of u_c from laminar flow always remains less than 10%.

The existence of a wide range of polymer concentrations at which the flow is laminar makes a clear distinction between two regimes where polymers play different dynamical roles. In the first regime the role of the polymers is to suppress turbulence and cause a reverse transition. As discussed in §4, the dynamics in this regime are dominated by the same flow structures as in the Newtonian case and polymers simply act to delay

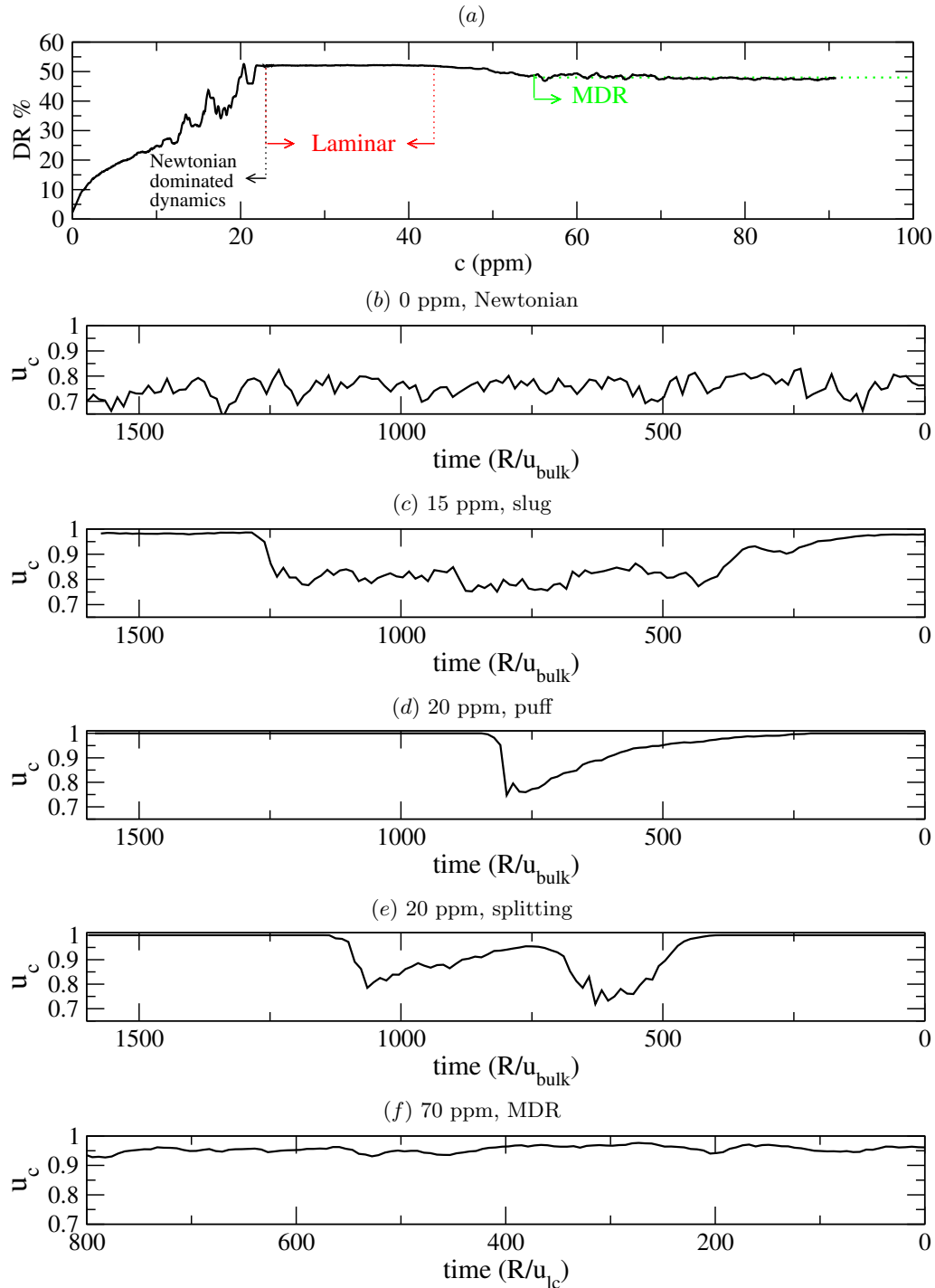


FIGURE 5. (a) Evolution of the drag reduction percentage DR% with increasing polymer concentration (expressed in parts per million by weight ppm) in the experiments of C,L&H for $Re = 3150$. (b) – (f) LDV measurements of the centreline velocity u_c illustrating the changes in the dynamics as polymer concentration increases.

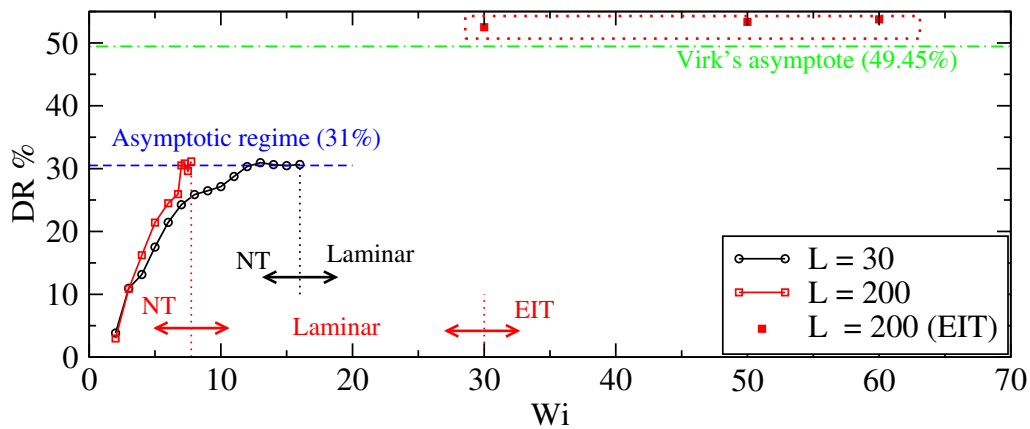


FIGURE 6. (Color online) Global scenario, in terms of drag reduction, obtained in simulations using a $10R$ long pipe and polymers with moderate ($L = 30$) and large extensibility ($L = 200$). The arrows delimit regions with distinct dynamical features. The acronyms NT and EIT denote the Newtonian dominated regime and the elasto-inertial turbulent regime, respectively. The data corresponding to the simulations of EIT presented in §6 is encircled by a (red) dotted rectangle. Note that the EIT regime was only found in the case of large polymer extensibility.

the transition scenario. In the second regime, for $c > 43$ ppm, the interplay between high polymer elasticity and inertial effects drives an instability, dubbed in Samanta et al. (2012) as elasto-inertial instability (EII), which results in a new turbulence type, elasto-inertial turbulence (EIT). As shown in fig. 5 (a), the drag reduction level associated with EIT is close to that of the Virk's asymptote and it remains unchanged as polymer concentration increases. These observations suggest that at these low Reynolds numbers EIT may be directly related to MDR.

An additional remark about EIT (and thus MDR) is that as seen in figure 5 (f), it is always space-filling and no spatio-temporal intermittency is observed in this regime. This is an important feature that can help distinguish realistic MDR dynamics from other regimes with similar statistical properties. An example of the latter are the puffs found prior to relaminarisation. We found in both simulations and experiments that the average friction coefficient and mean velocity profiles associated with these puffs are nearly identical to those at MDR (not shown). Hence, the circumstance that time averaged statistical quantities match those of MDR (main criterion to identify MDR in many earlier studies) is a necessary but not sufficient condition to identify this regime in numerical simulations. An analysis of the spatio-temporal dynamics must also be carried out to discern whether or not the simulated flows belong to the MDR regime.

6. Elasto-inertial turbulence

We have shown so far that our FENEP-NS simulations qualitatively reproduce the dynamics observed in experiments up to the point where relaminarisation occurs. The next question is therefore whether by increasing Wi beyond the relaminarisation threshold these simulations are also capable of capturing the EII and MDR. To address this

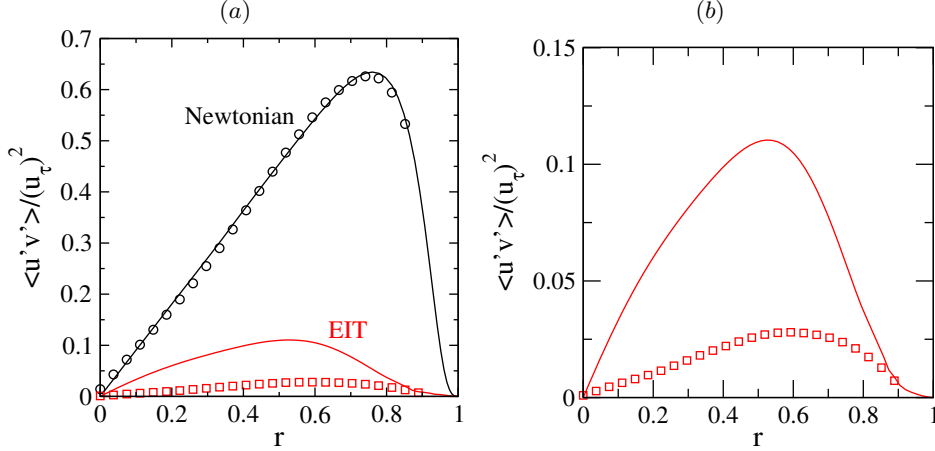


FIGURE 7. (Color online) (a) Reynolds shear stress $\langle -u'v' \rangle$, normalized with the friction velocity u_τ , for pure Newtonian turbulence and elasto-inertial turbulence in experiments (symbols) and simulations (solid lines). In simulations, the elasto-inertial turbulent state shown was computed at $Wi = 60$ for the LE case, whereas the experimental results correspond to a polymer concentration of 100 ppm, where the state of maximum drag reduction has already been achieved. Note that the experimental profiles do not extend all the way to the wall as reliable velocity measurements near the wall were not possible. (b) Zoom of (a) to facilitate comparison between experiments and simulations in the elasto-inertial turbulent regime.

question we have performed several simulations at Wi ranging from 20 to 80 in both the ME and LE cases. The pipe length was initially set again to $10R$. The simulations were initialized from the base flow, previously computed, which was perturbed by adding a pair of streamwise localized rolls ($v = A(g + rg')\cos(\theta)e^{-10\sin^2(\pi z/L_z)}$ and $w = Ag\sin(\theta)e^{-10\sin^2(\pi z/L_z)}$, where $g = (1 - r^2)^2$ and A is the amplitude of the disturbance). The results of these simulations, in terms of drag reduction, are shown in figure 6 (see squares encircled by the dotted rectangle), which extend figure 1 (a) to larger Wi . In all simulations carried out for the ME case, the energy of the disturbance grows initially due to the lift-up mechanism, but after approximately $150 R/u_{lc}$ time units it decays gradually with time and the flow fully relaminarises. For the LE case, however, we find that a secondary instability sets in for $Wi \geq 30$. While similarly to the ME case transient growth and subsequent decay in energy are initially observed, here the energy increases again as the time evolves and eventually saturates to a new flow state significantly less energetic than that of Newtonian type turbulence. A possible explanation for this behaviour is as follows. Due to the initial disturbance polymers are greatly stretched and accumulate a significant amount of elastic energy. In response to this stretch, polymers generate stresses which act to weaken and eventually suppress this turbulence. As the turbulence intensity decays, polymers relax and the elastic energy they store is progressively transferred to the fluid. As a result, the kinetic energy increases again and a new form of instability takes place.

Figure 7 (a) shows the time and area averaged Reynolds shear stress, $\langle -u'v' \rangle$, for Newtonian turbulence and elasto-inertial turbulence in experiments (symbols) and sim-

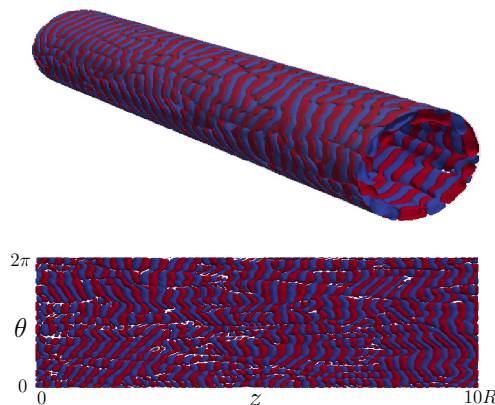


FIGURE 8. (Color online) Isosurfaces of the second invariant of the velocity gradient tensor $Q = -0.005$ and $Q = 0.005$ illustrating the topological structure of elasto-inertial turbulence. The top panel shows a 3D view of the pipe highlighting the near wall localisation of the structures. The bottom panel shows the characteristic pattern, with alternating regions of rotational and extensional/compressional behaviour, in a cylindrical section $\theta - z$ at the wall. The state shown corresponds to a simulation conducted at $Wi = 60$ for the LE case. The second invariant of the velocity gradient tensor is computed as $Q = (1/2)(\|\Omega\|^2 - \|\Gamma\|^2)$, where $\Omega = (1/2)(\nabla\mathbf{v} - \nabla\mathbf{v}^T)$ is the vorticity tensor and $\Gamma = (1/2)(\nabla\mathbf{v} + \nabla\mathbf{v}^T)$ is the rate-of-strain tensor.

ulations (solid lines). As seen, one of the prominent features of elasto-inertial turbulence as compared with Newtonian turbulence is its low Reynolds shear stress level. This is indicative that only a small fraction of the turbulent kinetic energy is produced by the conventional mechanisms of Newtonian turbulence, i.e. the self-sustaining cycle. Instead, turbulence here is primarily sustained by polymer stresses (Warholic *et al.* 1999). Note that while excellent agreement between simulations and experiments is obtained in the Newtonian case, the Reynolds shear stress level at EIT is larger by a factor of 3 in the simulations (see figure 7 (b)). This may be a consequence of the artificial diffusion used in the simulations, which is known to mitigate the polymer stresses, thereby leading to larger levels of Reynolds shear stress. The maximum of $\langle -u'v' \rangle$, which in the Newtonian case occurs near the wall, is located at an intermediate distance between the wall and the centreline, $r = 0.52$ and $r = 0.59$ in simulations and experiments, respectively. This is consistent with the thickening of the viscous buffer layer associated to high drag reduced flows (White *et al.* 2018). In contrast to Warholic *et al.* (1999), where zero Reynolds shear stresses were measured at high drag reduction, our results show low but finite values, in line with other simulations of EIT (Samanta *et al.* 2013). There is, however, a substantial difference in Re between our work (and other works on EIT) and that of Warholic *et al.* (1999), and so a direct comparison between these results may not be appropriate.

The topological structure of the new flow state is illustrated in figure 8 through isocontours of the second invariant of the velocity gradient tensor Q . Note that this quantity has been chosen to facilitate comparison with other works on EIT (Samanta *et al.* 2013; Dubief *et al.* 2013). Regions of intense vorticity ($Q > 0$, red) are found to alternate with

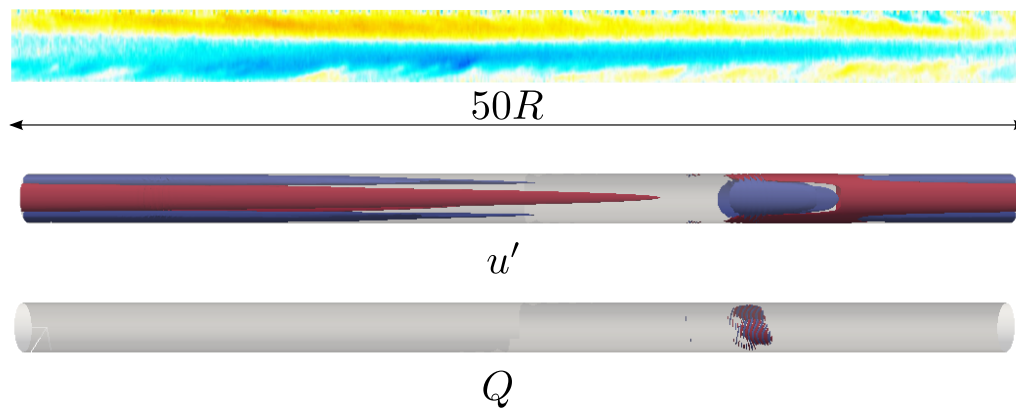


FIGURE 9. (Color online) The top panel shows the deviation of the streamwise velocity from the mean flow u' in a state of EIT for experiments conducted at $Re = 3150$. The velocity was measured using PIV in a pipe cross-section of nearly $6R$ in the axial direction. The image shown was obtained by assuming the Taylor’s frozen hypothesis, i.e. turbulence is advected downstream quickly and changes in time are slow. The intermediate and bottom panels show u' and Q respectively for a simulation performed at $Re = 3500$ and $Wi = 30$ in a $40R$ long pipe. Two isocontours $u' = \pm 0.1u'_{max}$ and $Q = \pm 0.005$ were used in each case.

strain-dominated regions ($Q < 0$, blue) creating a chaotic pattern of elongated spanwise oriented structures aligned in streamwise direction. The vortices are localized in the near wall region and are essentially two-dimensional with rotation being in the $r - z$ plane. We note that this spatial arrangement of structures in the near wall region is very different from Newtonian type turbulence, where the dominant structures are oriented in the streamwise direction. This flow state reproduces two essential features of MDR: the drag reduction level associated with this state remains nearly constant as Wi increases, and although the average friction factor ($f \sim 0.0047$) is slightly below that corresponding to the Virk’s asymptote ($f = 0.0051$), it is reasonably close to it. It should be noted that the Virk’s asymptote is a fit of empirical data collected from different experiments. As such, it should be used as an estimate for the friction of the MDR state rather than as a categorical result. All these observations are consistent with previous reports of elasto-inertial turbulence in channel flow simulations (Samanta *et al.* 2013; Dubief *et al.* 2013).

The top panel in figure 9 illustrates the typical flow structures of EIT in the experiments. It shows the streamwise velocity deviation with respect to the mean flow u' over a length of $50R$. Note that in the top panel the velocity was obtained from particle image velocimetry (PIV) in a section of nearly $6R$ in the axial direction and the Taylor’s Frozen turbulence hypothesis was then assumed to reconstruct the structures shown. As seen, the structure of EIT is clearly dominated by very elongated streaky structures aligned in the flow direction with a slight slope towards the centreline. The axial length of these structures is highly variable, ranging approximately from $50R$ to $200R$, being more elongated near the instability onset. As polymer concentration increases, the structures become shorter and increasingly more chaotic but still preserve their characteristic inclination.

Unlike in the simulations, vortical structures could not be resolved in the near wall region in the experiments. The vortical structures observed in the simulations are considerably weaker than Newtonian flow structures, which makes a detection in experiments difficult. In addition they are located close to the wall where the measurement accuracy is lower. In the simulations the problem is the opposite. Because of the Gauss-Lobatto-Chebyshev grid used in the radial direction the computational nodes are clustered near the wall, enabling an accurate resolution of the flow in this area. Nevertheless, the necessity of very dense grids in the streamwise direction to properly resolve the near wall structures makes it extremely costly to use axial domains sufficiently large as to capture the large scale structures observed in the experiments. A direct comparison of the structure of EIT between experiments and simulations is thus challenging. It is however tempting to investigate whether large scale structures can also be identified in simulations, and if their length approaches that of the structures in experiments as the computational domain is increased. To that extent, we have performed an additional simulation at $Wi = 30$ using a pipe of $40R$ in streamwise direction. EIT could only be captured transiently in this simulation and after approximately 2500 time units the flow went back to laminar. Nevertheless, some interesting dynamical aspects could be inferred from this simulation. As seen in the bottom panel of figure 9, if the same threshold $Q = \pm 0.005$ as in figure 8 is used, the near wall vortices appear localized over a short region of nearly $2R$ in the streamwise direction. Large scale streamwise velocity structures (see intermediate panel) seem to emerge from the area where the vortices are located and extend almost over the entire domain. These structures become thinner as they are followed downstream and take an arrow shape at the leading edge which closely resembles the inclination away from the wall observed in the experiments. This structural similarity between EIT in simulations and experiments suggests that the flow in both cases may be driven by the same instability. However, the precise dynamical relation between the small near wall structures and these elongated streaks still remains to be determined and will be the focus of a future investigation.

7. Conclusions

We have investigated numerically the dynamics of viscoelastic pipe flow at $Re = 3500$, where in the Newtonian case flows are fully turbulent (Barkley *et al.* 2015). In agreement with recent experimental observations, we find that the dynamics as Wi increases can be categorized in two regimes. The first regime takes place for low-to-moderate Wi and the dynamics are essentially of the Newtonian type. The influence of polymers on this regime manifests itself as a reverse transition: the flow goes from the turbulent to the laminar state following the same stages as in the Newtonian laminar-turbulence transition, but in reverse order, i.e. fully turbulent, slugs, puff splitting, puffs and laminar. The second regime occurs at large Wi and could only be captured in the simulations when considering polymers with very large extensibility. The amount of drag reduction associated with this regime is near that of the Virk's asymptote and remains unchanged as Wi increases. These

properties are consistent with the state of MDR, suggesting that, at these low Reynolds numbers, elasto-inertial turbulence and MDR may correspond to the same flow state. Separating the Newtonian and elasticity dominated regimes, there is a significant range of Wi for which the flow relaminarises regardless of the initial condition. The existence of this laminar regime implies that the dynamics at the elasticity dominated regime is disconnected from Newtonian type turbulence, and consequently it would have to originate from a separate instability (EII). The robustness of the described dynamics has been recently corroborated by Shekar *et al.* (2019), who also reported relaminarisation followed by a second transition leading to EIT in simulations of channel flow at low Reynolds numbers.

We would like to emphasize again that the results discussed in this paper correspond to simulations and experiments at Reynolds numbers near transition. Hence, our conclusions only apply to this regime. At larger Re , the relaminarisation reported here does not take place and elasto-inertial turbulence coexists with Newtonian turbulence (Choueiri *et al.* 2018; White *et al.* 2018) at high Wi . It can therefore be expected that the properties of MDR will change with increasing Re , supporting the non-universality of this state (White *et al.* 2012).

We also show that MDR in simulations cannot be identified based on average profiles and friction values alone. While in the hibernating regime these quantities are close to those of MDR, larger domain studies identify this regime as spatio temporal intermittency and as part of a reverse transition scenario. The asymptotic MDR regime is only approached for even larger Weissenberg numbers.

REFERENCES

- BARKLEY, D., SONG, B., MUKUND, V., LEMOULT, G., AVILA, M. & HOF, B. 2015 The rise of fully turbulent flow. *Nature* **526** (7574), 550–553.
- BENZI, R., DE ANGELIS, E., L'VOV, V. S., PROCACCIA, I. & TIBERKEVICH, V. 2006 Maximum drag reduction asymptotes and the cross-over to the newtonian plug. *Journal of Fluid Mechanics* **551**, 185195.
- BERIS, A. N. & DIMITROPOULOS, C. D. 1999 Pseudospectral simulation of turbulent viscoelastic channel flow. *Computer Methods in Applied Mechanics and Engineering* **180** (3), 365 – 392.
- BIRD, R., DOTSON, P. & JOHNSON, N. 1980 Polymer solution rheology based on a finitely extensible beadspring chain model. *Journal of Non-Newtonian Fluid Mechanics* **7** (2), 213 – 235.
- CHOUERI, G. H., LOPEZ, J. M. & HOF, B. 2018 Exceeding the asymptotic limit of polymer drag reduction. *Phys. Rev. Lett.* **120**, 124501.
- DUBIEF, Y., TERRAPON, V. E. & SORIA, J. 2013 On the mechanism of elasto-inertial turbulence. *Physics of Fluids* **25** (11), 110817.
- ELBING, B. R., PERLIN, M., DOWLING, D. R. & CECCIO, S. L. 2013 Modification of the mean near-wall velocity profile of a high-reynolds number turbulent boundary layer with the injection of drag-reducing polymer solutions. *Physics of Fluids* **25** (8), 085103.
- GIUDICE, F. D., HAWARD, S. J. & SHEN, A. Q. 2017 Relaxation time of dilute polymer solutions: A microfluidic approach. *Journal of Rheology* **61** (2), 327–337.

- HOF, B., DE LOZAR, A., AVILA, M., TU, X. & SCHNEIDER, T. M. 2010 Eliminating turbulence in spatially intermittent flows. *Science* **327** (5972), 1491–1494.
- LI, C.-F., SURESHKUMAR, R. & KHOMAMI, B. 2006 Influence of rheological parameters on polymer induced turbulent drag reduction. *Journal of Non-Newtonian Fluid Mechanics* **140** (1), 23 – 40, special Issue on the XIVth International Workshop on Numerical Methods for Non-Newtonian Flows, Santa Fe, 2005.
- LITTLE, R. C. & WIEGARD, M. 1970 Drag reduction and structural turbulence in flowing polyox solutions. *Journal of Applied Polymer Science* **14** (2), 409–419.
- L'VOV, V. S., POMYALOV, A., PROCACCIA, I. & TIBERKEVICH, V. 2004 Drag reduction by polymers in wall bounded turbulence. *Phys. Rev. Lett.* **92**, 244503.
- ORSZAG, S. A. & PATERA, A. T. 1983 Secondary instability of wall-bounded shear flows. *J. Fluid Mech.* **128**, 347–385.
- PTASINSKY, P. K., BOERSMA, B. J., NIEUWSTADT, F. T. M., HULSEN, M. A., VAN DEN BRULE, B. H. A. A. & HUNT, J. C. R. 2003 Turbulent channel flow near maximum drag reduction: simulations, experiments and mechanisms. *J. Fluid Mech.* **490**, 251291.
- RAM, A. & TAMIR, A. 1964 Structural turbulence in polymer solutions. *Journal of Applied Polymer Science* **8** (6), 2751–2762.
- SAMANTA, D., DUBIEF, Y., HOLZNER, M., SCHÄFER, C., MOROZOV, A. N., WAGNER, C. & HOF, B. 2013 Elasto-inertial turbulence. *Proceedings of the National Academy of Sciences* **110** (26), 10557–10562.
- SHEKAR, A., MCMULLEN, R. M., WANG, S.-N., MCKEON, B. J. & GRAHAM, M. D. 2019 Critical-layer structures and mechanisms in elastoinertial turbulence. *Phys. Rev. Lett.* **122**, 124503.
- SHI, L., RAMPP, M., HOF, B. & AVILA, M. 2015 A hybrid mpi-openmp parallel implementation for pseudospectral simulations with application to taylorcouette flow. *Computers & Fluids* **106**, 1 – 11.
- SID, S., TERRAPON, V. E. & DUBIEF, Y. 2018 Two-dimensional dynamics of elasto-inertial turbulence and its role in polymer drag reduction. *Phys. Rev. Fluids* **3**, 011301.
- SREENIVASAN, K. R. & WHITE, C. M. 2000 The onset of drag reduction by dilute polymer additives, and the maximum drag reduction asymptote. *Journal of Fluid Mechanics* **409**, 149164.
- SURESHKUMAR, R., BERIS, A. N. & HANDLER, R. A. 1997 Direct numerical simulation of the turbulent channel flow of a polymer solution. *Physics of Fluids* **9** (3), 743–755.
- TOMS, B. A. 1948 Some observation on the flow of linear polymer solutions through straight tubes at large Reynolds numbers. In *Proc. 1st Intl. Congr. on Rheology*, , vol. Vol. II, pp. 135–141.
- VIRK, P., MICKLEY, H. & SMITH, K. 1970 The ultimate asymptote and mean flow structure in toms' phenomenon. *J. Appl. Mech.* **37** (2), 488–493.
- WANG, S.-N., SHEKAR, A. & GRAHAM, M. D. 2017 Spatiotemporal dynamics of viscoelastic turbulence in transitional channel flow. *Journal of Non-Newtonian Fluid Mechanics* **244**, 104 – 122.
- WARHOLIC, M., MASSAH, H. & HANRATTY, T. 1999 Influence of drag-reducing polymers on turbulence: effects of reynolds number, concentration and mixing. *Experiments in fluids* **27** (5), 461–472.
- WHITE, C. M., DUBIEF, Y. & KLEWICKI, J. 2012 Re-examining the logarithmic dependence of the mean velocity distribution in polymer drag reduced wall-bounded flow. *Physics of Fluids* **24** (2), 021701.

- WHITE, C. M., DUBIEF, Y. & KLEWICKI, J. 2018 Properties of the mean momentum balance in polymer drag-reduced channel flow. *Journal of Fluid Mechanics* **834**, 409433.
- WHITE, C. M. & MUNGAL, M. G. 2008 Mechanics and prediction of turbulent drag reduction with polymer additives. *Annual Review of Fluid Mechanics* **40** (1), 235–256.
- WILLIS, A. P. 2017 The openpipeflow navierstokes solver. *SoftwareX* **6**, 124 – 127.
- WYGNANSKI, I. J. & CHAMPAGNE, F. H. 1973 On transition in a pipe. part 1. the origin of puffs and slugs and the flow in a turbulent slug. *Journal of Fluid Mechanics* **59** (2), 281335.
- XI, L. & GRAHAM, M. D. 2010*a* Active and hibernating turbulence in minimal channel flow of newtonian and polymeric fluids. *Phys. Rev. Lett.* **104**, 218301.
- XI, L. & GRAHAM, M. D. 2010*b* Turbulent drag reduction and multistage transitions in viscoelastic minimal flow units. *J. Fluid Mech.* **647**, 421452.
- XI, L. & GRAHAM, M. D. 2012*a* Dynamics on the laminar-turbulent boundary and the origin of the maximum drag reduction asymptote. *Phys. Rev. Lett.* **108**, 028301.
- XI, L. & GRAHAM, M. D. 2012*b* Intermittent dynamics of turbulence hibernation in newtonian and viscoelastic minimal channel flows. *Journal of Fluid Mechanics* **693**, 433472.